



HAL
open science

Plasmonic and metallic optical properties of Au/SiO₂ metal-insulator films

Yann Battie, Aotmane En Naciri, Michel Vergnat

► **To cite this version:**

Yann Battie, Aotmane En Naciri, Michel Vergnat. Plasmonic and metallic optical properties of Au/SiO₂ metal-insulator films. *Journal of Applied Physics*, 2017, 122 (21), pp.213101. 10.1063/1.5003302 . hal-02168859

HAL Id: hal-02168859

<https://hal.science/hal-02168859v1>

Submitted on 29 Jun 2019

HAL is a multi-disciplinary open access archive for the deposit and dissemination of scientific research documents, whether they are published or not. The documents may come from teaching and research institutions in France or abroad, or from public or private research centers.

L'archive ouverte pluridisciplinaire **HAL**, est destinée au dépôt et à la diffusion de documents scientifiques de niveau recherche, publiés ou non, émanant des établissements d'enseignement et de recherche français ou étrangers, des laboratoires publics ou privés.

Plasmonic and metallic optical properties of Au/SiO₂ metal-insulator films

Yann Battie,^{1,a)} Aotmane En Naciri,¹ and Michel Vergnat²

¹LCP-A2MC, Institut Jean Barriol, Université de Lorraine, 1 Bd Arago, 57070 Metz, France

²Université de Lorraine, Institut Jean Lamour, UMR7198, Nancy F-54011, France

(Received 5 September 2017; accepted 13 November 2017; published online 5 December 2017)

In this paper, the optical properties and the growth mechanism of Au/SiO₂ metal-insulator films (MIFs) are investigated by combining ellipsometry and transmission electron microscopy. The ellipsometric measurements, analyzed by using effective medium theories, show that the growth mechanism involves a Volmer-Weber growth mode while the morphology and the optical properties of Au/SiO₂ MIFs are directly related to the percolation of the Au nanostructures. Indeed, below the percolation threshold of Au, the MIFs consist of ellipsoidal Au inclusions embedded in a SiO₂ matrix. These insulating films present anisotropic plasmonic properties, attributed to the asymmetric interactions between nanoparticles (NPs), which can be modeled according to the interacted shape distributed nanoparticle effective medium theory. At the percolation threshold of Au, an insulator-to-metal transition is observed. The MIFs simultaneously exhibit plasmonic and metallic optical properties, which can be described by the Bruggeman theory. The density of free electrons increases and the MIFs become more and more conductive as the Au volume fraction increases. We also demonstrate that for a high Au volume fraction, Bruggeman and Maxwell Garnett theories converge toward the same results, suggesting that the film is composed of isolated SiO₂ inclusion embedded in a gold matrix. *Published by AIP Publishing.* <https://doi.org/10.1063/1.5003302>

I. INTRODUCTION

Thin films, composed of a metal-insulator mixture, exhibit unique optical and electrical properties that deviate from those of the bulk metals.¹ Indeed, depending on their composition, these metal-insulator films (MIFs) can have metallic or insulating behavior.^{2–6} Moreover, as reported by several authors, MIFs can exhibit strong plasmonic effects^{7–10} and local electric field enhancement.^{11–13} Therefore, they can be considered as a building block for nonlinear materials,^{14,15} new metamaterial devices,¹⁶ plasmonic sensors,^{17–19} or transparent screens.²⁰

Usually, MIFs are characterized by electrical conductivity or transmission spectroscopy measurements. However, conductivity measurements cannot be made for MIFs integrated into devices such as a metallic film sandwiched between two insulating layers. In addition, due to their low transmission coefficient, transmission spectroscopy fails to characterize MIFs when their thickness and their volume fraction are too high.

Spectroscopic ellipsometry is a non-destructive indirect optical characterization tool, which is highly sensitive to the optical properties of thin films. Ellipsometry was recently exploited to monitor the nucleation of silver or gold NPs on a surface,^{21,22} the gradient of volume fraction of silver nanoparticles (NPs) in a silica film,²³ and the percolation of gold or silver thin films.^{2,24} As ellipsometry is an indirect characterization, a physical model, which takes into account the optical properties of the film, must be established to exploit the ellipsometric data. Hövel *et al.*²⁵ have demonstrated that close to the percolation threshold, the dielectric function of

gold films is a sum of Drude- and Lorentz-terms, which describe the contribution of free electrons and the plasmon band, respectively. However, as pointed out by Lončarić *et al.*,²⁶ this dielectric function requires the determination of a large number of free parameters. This leads to erroneous and unphysical solutions, which come from the correlations between the film thickness and dielectric function. To address this issue, effective medium theories¹ can be used to describe the optical properties of MIFs with a limited number of free parameters. However, several effective medium theories have been developed depending on the morphology of the film. The Bergman effective medium theory is based on the determination of the spectral representation function (SRF) which depends on a large number of parameters such as the interactions between NPs or the NP size and shape distributions.²⁷ However, this multivariate dependence makes unclear the interpretation of the SRF. The Maxwell Garnett theory (MG),²⁸ which is based on the Lorentz local field, is often used to predict the plasmon band of monodispersed spherical NPs embedded in a homogeneous matrix. However, this theory fails to model the optical properties of real materials composed of NPs distributed in size and shape. Several attempts have been made to date to introduce the effects of nanoparticle size²⁹ and shape distributions in the effective medium theory.^{30–34} These theories only consider well-defined NPs and fail to describe the optical properties of the percolated and interconnected metallic network. The Bruggeman theory [Bruggeman effective medium approximation (BEMA)]¹ avoids this problem by treating the constituents symmetrically. The BEMA was previously used to simulate the optical properties of the nanoporous gold network.³⁵ However, according to Yagil *et al.*,³⁶ the BEMA does not accurately describe the optical properties of MIFs

^{a)}Author to whom correspondence should be addressed: yann.battie@univ-lorraine.fr

close to their percolation threshold. Thus, the choice of the effective medium theory does not reach a consensus yet.

In this paper, the optical properties and the growth mechanism of SiO₂/Au films are investigated by combining ellipsometry and transmission electron microscopy (TEM). The growth of these MIFs is interpreted according to a Volmer-Weber growth mechanism followed by a Frank-Van der Merwe growth mode. The ellipsometric spectra are analyzed by using three effective medium theories: the interacted shape distributed nanoparticle effective medium theory (ISDEMT), the MG theory, and the BEMA theory. We demonstrate that the choice of the effective medium theory depends on the volume fraction of Au. This behavior is interpreted in terms of percolation of the discontinuous metallic network. Indeed, beyond the percolation threshold, the optical properties of MIFs are well reproduced by the ISDEMT theory. These MIFs exhibit anisotropic plasmonic properties, which are mainly influenced by the NP shape distribution and the anisotropic interaction between NPs. At the percolation, threshold, which occurs for the Au volume fraction estimated at 36%, an insulator-to-metal transition is observed. The MIFs simultaneously exhibit plasmonic and metallic optical properties, which can be described by the BEMA theory. However, for a higher concentration than the percolation threshold of SiO₂, the BEMA and the MG theories converge toward the same results. Indeed, these MIFs can be view as a SiO₂ inclusion in the Au matrix.

II. EXPERIMENTAL SECTION

MIF films were prepared by successive evaporation of fused silica performed by an electron-beam gun and thermal evaporation of Au from a tungsten thermal cell. With an acceleration voltage equal to 10 kV and an electronic current equal to 15 mA, the power of the electron beam gun was 150 W to evaporate the SiO₂ powder. The intensity of the current through the tungsten boat was 140 A to evaporate the Au grains. The pressure is lower than 10⁻⁶ Torr during the evaporation process, the ultimate vacuum of the evaporation chamber being 10⁻⁸ Torr. The deposition rate is controlled by a quartz microbalance system and is equal to 0.1 nm s⁻¹ for SiO₂ and 0.05 nm s⁻¹ for Au. The (100) silicon substrates were maintained at 100 °C.

The multilayer structure was studied by transmission electron microscopy (TEM), with a Philips CM200 microscope. The acceleration voltage was 200 kV and bright field imaging was used to get the images. By using a microcleavage technique, we collected some fragments on an electron microscope grid. The observation of the sample in the cross section visually confirms the modulation.

Standard ellipsometric measurements are performed in air at room temperature using a phase-modulated ellipsometer (UVISEL Horiba). The measurements are recorded in the 0.6–4.7 eV spectral range at four angles of incidence: 60°, 65°, 70°, and 75°. Ellipsometry measures the changes in the polarization state between the incident and reflected light on the samples. The measured ellipsometric angles (ψ , Δ) are related to the ratio of the Fresnel reflection coefficients of

the sample, r_p and r_s , of p-polarized and s-polarized light, respectively,

$$\frac{r_p}{r_s} = \tan \Psi e^{i\Delta}. \quad (1)$$

Phase-modulated ellipsometer measures two parameters, I_s and I_c , which are related to the ellipsometric angles Ψ and Δ by the following equations:

$$I_s = \sin 2\Psi \sin \Delta, \quad (2)$$

$$I_c = \sin 2\Psi \cos \Delta. \quad (3)$$

III. THEORY

A. Maxwell Garnett effective medium theory

The Maxwell Garnett effective medium theory (MG)²⁸ describes the optical properties of an isotropic and homogeneous composite material, which consists of spherical monodispersed nanoparticles embedded in a matrix. This material is modeled as a homogeneous medium characterized by an effective dielectric function ϵ_{eff} given by

$$\frac{\epsilon_{eff} - \epsilon_m}{\epsilon_{eff} + 2\epsilon_m} = f \frac{\epsilon_{np} - \epsilon_m}{\epsilon_{np} + 2\epsilon_m}, \quad (4)$$

where ϵ_m and ϵ_{np} are the dielectric functions of the matrix and the nanoparticles respectively, while f is the volume fraction of NPs. The NP size must be smaller than the wavelength to satisfy the dipolar approximation. In addition, the interparticle distance must be sufficiently high to neglect the interaction between nanoparticles.

B. Interacted shape distributed nanoparticle effective medium theory (ISDEMT)

We consider a material composed of ellipsoidal nanoparticles distributed in shape and embedded in a matrix. The optical properties of this composite material are described by an effective dielectric tensor $[\epsilon_{eff}]$. The macroscopic polarization \mathbf{P} of the composite material is related to the macroscopic electric fields \mathbf{E}

$$\mathbf{P} = \epsilon_0([\epsilon_{eff}] - \epsilon_m)\mathbf{E}, \quad (5)$$

where ϵ_0 is the vacuum permittivity. By assuming that the interparticle distance is large enough to use point dipole approximation, the macroscopic polarization is also defined as the total dipolar momentum \mathbf{p}_k of nanoparticles per unit volume V

$$\mathbf{P} = \frac{1}{V} \sum_k \mathbf{p}_k. \quad (6)$$

The dipolar momentum \mathbf{p}_k of the NP k is calculated from the polarizability tensor (α_k) and the local electric field $\mathbf{E}_{loc,k}$ applied on the NP k

$$\mathbf{p}_k = \epsilon_0 \epsilon_m V_k [\alpha_k] \mathbf{E}_{loc,k}, \quad (7)$$

where V_k is the volume of the NP k . In the following, we assume an in-plane orientation of NPs. The polarizability tensor of the nanoparticle k is given by

$$[\alpha_k] = \begin{pmatrix} \cos \theta_k & -\sin \theta_k & 0 \\ \sin \theta_k & \cos \theta_k & 0 \\ 0 & 0 & 1 \end{pmatrix} \begin{pmatrix} \alpha_{k,1} & 0 & 0 \\ 0 & \alpha_{k,2} & 0 \\ 0 & 0 & \alpha_{k,3} \end{pmatrix} \times \begin{pmatrix} \cos \theta_k & \sin \theta_k & 0 \\ -\sin \theta_k & \cos \theta_k & 0 \\ 0 & 0 & 1 \end{pmatrix}, \quad (8)$$

where θ_k is the angle which defines the in-plane orientation of the ellipsoidal NP. The NP polarizability along the NP axis $l = 1, 2, 3$ is given by

$$\alpha_{k,l} = \frac{\varepsilon_{np} - \varepsilon_m}{\varepsilon_m + L_{k,l}(\varepsilon_{np} - \varepsilon_m)}, \quad (9)$$

where ε_{np} is the dielectric function of NPs. $L_{k,l}$ is the depolarization factor along the NP axis l . This parameter only depends on the NP shape

$$L_{k,l} = \frac{a_{k,1}a_{k,2}a_{k,3}}{2} \times \int_0^\infty \frac{dq}{(q + a_{k,l}^2) \sqrt{(q + a_{k,1}^2)(q + a_{k,2}^2)(q + a_{k,3}^2)}}, \quad (10)$$

where $a_{k,l}$ is the half length of the principal axes of the NP k . The local electric field is the sum of the macroscopic electric field \mathbf{E} and the field produced by the other NPs $\mathbf{E}_{i,k}$

$$\mathbf{E}_{loc,k} = \mathbf{E} + \sum_{i \neq k} \mathbf{E}_{i,k}. \quad (11)$$

The second term of Eq. (11), which describes the dipolar interactions between NPs, is given by

$$\mathbf{E}_{i,k} = \frac{1}{\varepsilon_0 \varepsilon_m} A_{i,k} \mathbf{p}_i, \quad (12)$$

with

$$A_{ik} = \frac{1}{4\pi r_{ik}^3} \begin{pmatrix} 3x_{ik}^2 - 1 & 3x_{ik}y_{ik} & 3x_{ik}z_{ik} \\ 3x_{ik}y_{ik} & 3y_{ik}^2 - 1 & 3y_{ik}z_{ik} \\ 3x_{ik}z_{ik} & 3y_{ik}z_{ik} & 3z_{ik}^2 - 1 \end{pmatrix}, \quad (13)$$

$\mathbf{r}_{ik} = \mathbf{r}_i - \mathbf{r}_k$ is the vector, which links the NP i and the NP k . r_{ik} is the norm of this vector while x_{ik} , y_{ik} , and z_{ik} are the coordinates of the \mathbf{r}_{ik}/r_{ik} unit vector.

We assume that NPs have a homogeneous in-plane organization. In other words, the NPs are exposed to the same local field ($\mathbf{E}_{loc} = \mathbf{E}_{loc,k}$), whose expression is deduced from Eqs. (7), (11), and (12)

$$\mathbf{E}_{loc} = \left(1 - \sum_{i \neq k} V_i A_{i,k} [\alpha_i]\right)^{-1} \mathbf{E}, \quad (14)$$

where $\mathbf{1}$ is the 3×3 identity matrix. The effective dielectric tensor of the composite is obtained by combining Eqs. (5) and (14)

$$[\varepsilon_{eff}] = \varepsilon_m \left(1 + \sum_k \frac{V_k}{V} [\alpha_k] \left(1 - \sum_{i \neq k} V_i A_{i,k} [\alpha_i]\right)^{-1}\right). \quad (15)$$

This effective dielectric tensor takes into account the organization and the shape distribution of ellipsoidal NPs as well as the dipolar interaction between them. In the case of isotropic 3D materials composed of highly diluted monodisperse spherical NPs, this equation is equivalent to the Maxwell Garnett Equation (4).

C. Bruggeman theory

The Bruggeman effective medium approximation (BEMA)¹ describes the optical properties of the composite medium, where inclusions and the host material share the same roles. This model is often used when both media have a similar volume fraction. The BEMA effective dielectric function is determined by considering that the total dipole moment of the effective medium equals to 0. The total dipole moment is calculated in the framework of non-interacting dipoles. The BEMA is based on the following equation:

$$0 = f_a \frac{\varepsilon_a - \varepsilon_{eff}}{f_s \varepsilon_a + (1 - f_s) \varepsilon_{eff}} + f_b \frac{\varepsilon_b - \varepsilon_{eff}}{f_s \varepsilon_b + (1 - f_s) \varepsilon_{eff}}, \quad (16)$$

where ε_a and ε_b are the dielectric functions of the constituents while f_a and f_b are their volume fractions. f_s is the volume fraction corresponding to the percolation threshold of materials. This equation is symmetric so, the role of the matrix and the nanoparticles can be inverted.

IV. RESULTS AND DISCUSSION

Four MIFs denoted F1, F2, F3, and F4 are investigated. These MIFs are composed of three layers deposited on a silicon substrate: a SiO₂ top layer (L1), a SiO₂/Au layer (L2), and a SiO₂ bottom layer (L3). The nominal thicknesses of the Au layer of F1, F2, F3, and F4, determined by a quartz microbalance system with the hypothesis of a density of material equal to the density of the bulk material, were estimated to be 2.8, 5.6, 11.2, and 22.4 nm, respectively, whereas the SiO₂ barrier thickness was maintained constant and equal to 50 nm. The details of the F1 and F2 morphology are obtained from transmission electron microscopy (TEM) observations of the film surface [$(\mathbf{e}_1, \mathbf{e}_2)$ plane] and cross section [$(\mathbf{e}_1, \mathbf{e}_3)$ plane] (Fig. 1). F1 is composed of a monolayer of nonspherical Au inclusions sandwiched between two SiO₂ layers. The thickness of the nanoparticle layer (L2) is estimated at $12 \text{ nm} \pm 2 \text{ nm}$, while the thicknesses of the top (L1) and the bottom (L2) SiO₂ layers are $56 \text{ nm} \pm 2 \text{ nm}$ and $52 \text{ nm} \pm 2 \text{ nm}$, respectively. The surface density of NPs is about 50%. By assuming that this layer is composed of ellipsoidal Au inclusions, which have the same size along the \mathbf{e}_3 axis, their volume fraction can be estimated at 33%. Contrary to F1, the middle layer of F2 is composed of

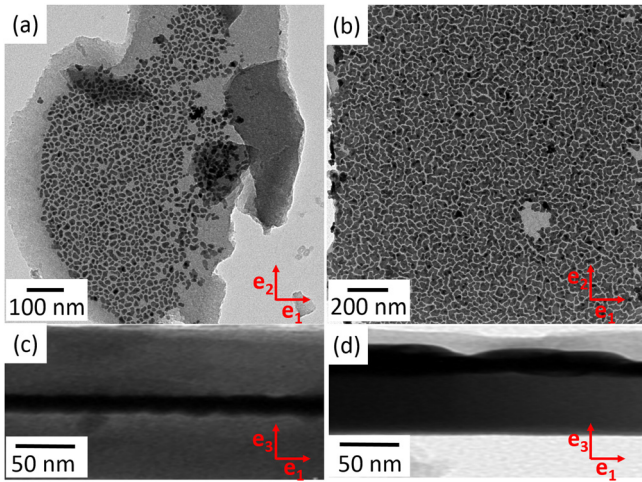


FIG. 1. (a) and (b) Top view and (c) and (d) cross section TEM images of (a)–(c) F1 and (b)–(d) F2.

percolated Au nanostructures, which have a pseudodendritic shape. The surface density of the nanostructure and the thickness of this layer are estimated at 75% and 16 nm, respectively. The fractal dimensions of F1 and F2, determined from the relationship between the perimeter and the area of NPs,³⁷ are estimated at 1.2 and 1.6, respectively. This result suggests that F2 is composed of fractal nanostructures.

The distribution of the minimum and maximum apparent Feret diameters of F1 NPs, defined as the smallest and the longest dimensions of NPs in the $(\mathbf{e}_1, \mathbf{e}_2)$ plane, are shown in Fig. 2(a). These distributions are obtained from a statistical analysis of 580 NPs. In the first approximation, the distribution of the Feret diameters of NPs follows Gaussian distributions centered at 9 nm and 14 nm, respectively. This size is large enough to neglect the confinement effect, which comes from the limitation of the mean free path of free

electrons by the NP surface. In addition, the nanoparticle size is sufficiently small to model their optical properties by using the quasistatic approximation. The apparent aspect ratio distribution of F1 NPs in the $(\mathbf{e}_1, \mathbf{e}_2)$ plane, shown in Fig. 2(b), enables a quantitative estimation of the NP shape distribution. In the following, the NP aspect ratio is defined as the ratio between the minimum and maximum apparent Feret diameters in the $(\mathbf{e}_1, \mathbf{e}_2)$ plane. F1 NPs have a broad in-plane aspect ratio distribution centered at 0.65 with a 0.2 standard deviation. As shown in Fig. 2(c), the distribution of the angle θ between \mathbf{e}_1 and the apparent major axis of the NPs in the $(\mathbf{e}_1, \mathbf{e}_2)$ plane confirms that nanoparticles are randomly oriented in the $(\mathbf{e}_1, \mathbf{e}_2)$ plane. To investigate the organization of NPs, we also calculate the two-dimensional pair correlation function of NPs by using the following equation:

$$g(r) = \frac{1}{2\pi r \sigma} \frac{1}{dr} \frac{1}{N_{np} - 1} \sum_{m=1}^{N_{np}} n_m(r), \quad (17)$$

where σ is the surface density of NPs, while N_{np} is the number of NPs in the system. $n_m(r)$ is the number of NPs contained in the ring of radius r and thickness dr , centered on the NP m . The two-dimensional pair correlation function of NPs, shown in Fig. 2(d), can be assimilated to a step-like function, suggesting that nanoparticles are homogeneously distributed in the $(\mathbf{e}_1, \mathbf{e}_2)$ plane. The interparticle distance is estimated from the $g(r)$ function at 14 nm. Indeed, a broad peak is observed for this distance. The absence of a second peak in the two-dimensional pair correlation function confirms that NPs are not organized in the $(\mathbf{e}_1, \mathbf{e}_2)$ plane.

Spectroscopic ellipsometric measurements performed on F1, F2, F3, and F4 are shown in Figs. 3 and 4. The ellipsometric spectra are sample dependent, confirming that ellipsometry is sufficiently sensitive to detect the variations of the nanostructure morphology and the composition of the

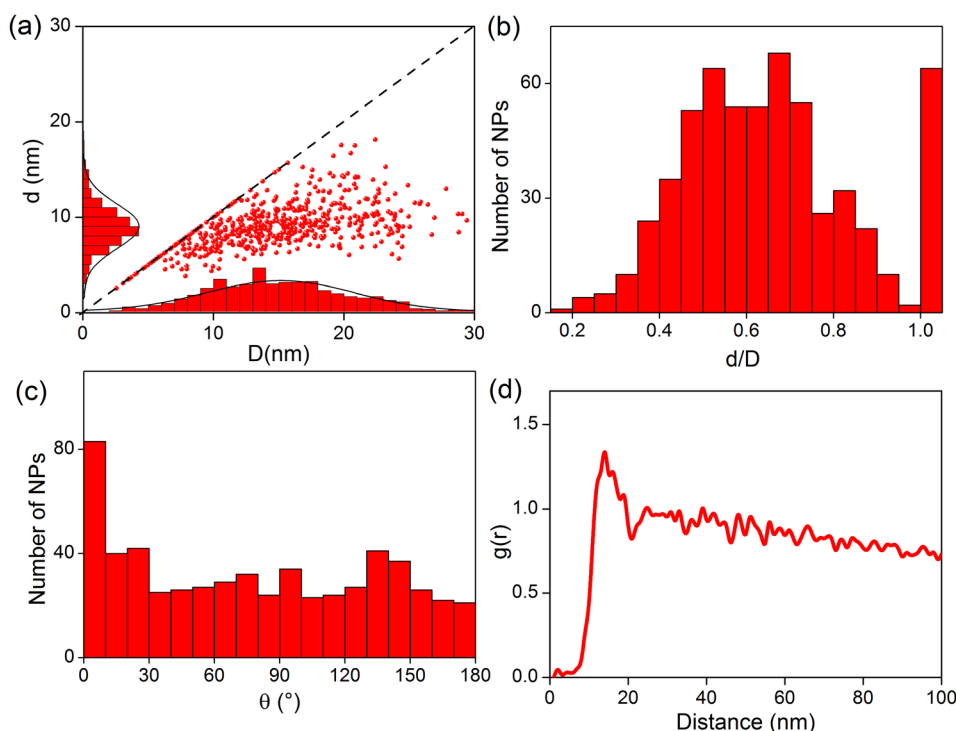


FIG. 2. (a) Distributions of the apparent Feret diameters and (b) aspect ratio of F1 NPs in the $(\mathbf{e}_1, \mathbf{e}_2)$ plane measured by TEM. (c) Distribution of the angle θ between \mathbf{e}_1 and the apparent major axis of F1 NPs in the $(\mathbf{e}_1, \mathbf{e}_2)$ plane. (d) Two-dimensional pair correlation function of F1 NPs in the $(\mathbf{e}_1, \mathbf{e}_2)$ plane.

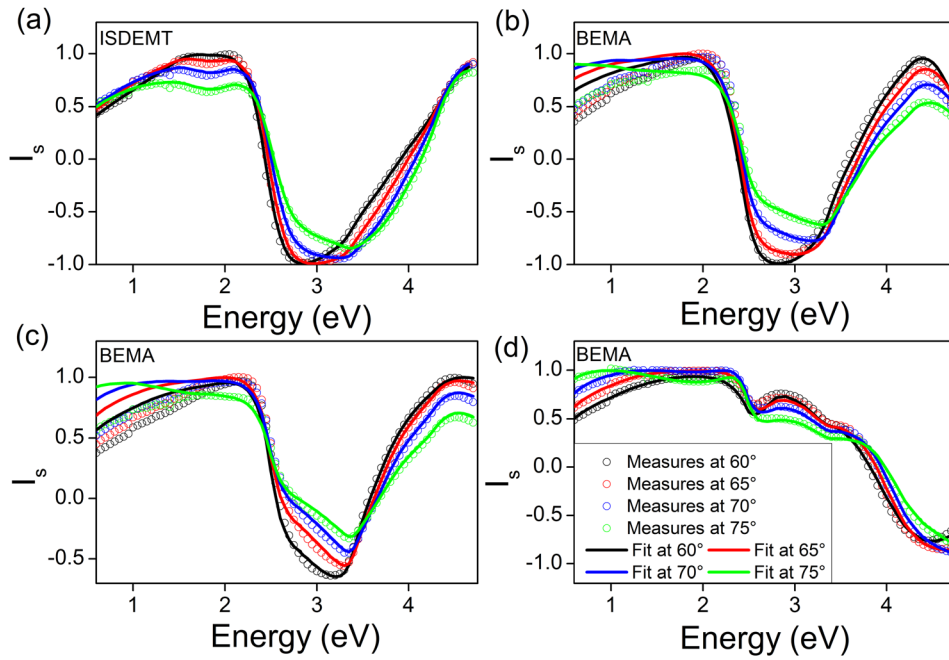


FIG. 3. Comparison between the measured (symbol) and calculated (solid lines) I_s ellipsometric parameters of (a) F1, (b) F2, (c) F3, and (d) F4. The measurements are performed at 4 angles of incidence: 60°, 65°, 70°, and 75°.

SiO_2/Au layer. To extract the optical properties of nanocomposite layers from ellipsometric data, an optical model must be introduced. The sample is represented as a stack of three sublayers: a pure silica top sublayer (L1), an intermediate sublayer (L2) made of a mixture of silica and Au nanostructures, and finally, a pure silica bottom sublayer (L3) on the silicon substrate. The dielectric functions of silica and gold are given by Palik.³⁸ The optical properties of L2 are described by an effective dielectric function calculated from the MG and the BEMA theories or an effective dielectric tensor calculated from the ISDEMT theory. To exploit each ellipsometric spectra from the MG theory, 4 free parameters are determined by using the Levenberg-Maquardt algorithm: the volume fraction f of Au nanostructures in L2, and the

thicknesses of the sublayers. The modeling with the BEMA theory is performed in two steps: first, we determine the percolation threshold of nanostructures by fitting simultaneously the ellipsometric spectra of all samples. Indeed, we assume that the percolation threshold f_s remains constant for all samples. The volume fraction at the percolation threshold f_s is estimated at 36%. In the second step, the ellipsometric spectra of each sample are analyzed separately by fitting 4 free parameters: the volume fraction f of Au nanostructures in L2, and the thicknesses of the sublayers. Note that the percolation threshold is set to the value obtained in step 1. In the case of F1, we also consider that the optical properties of L2 can be described by an effective dielectric tensor calculated from the ISDEMT without free parameters. Indeed, the

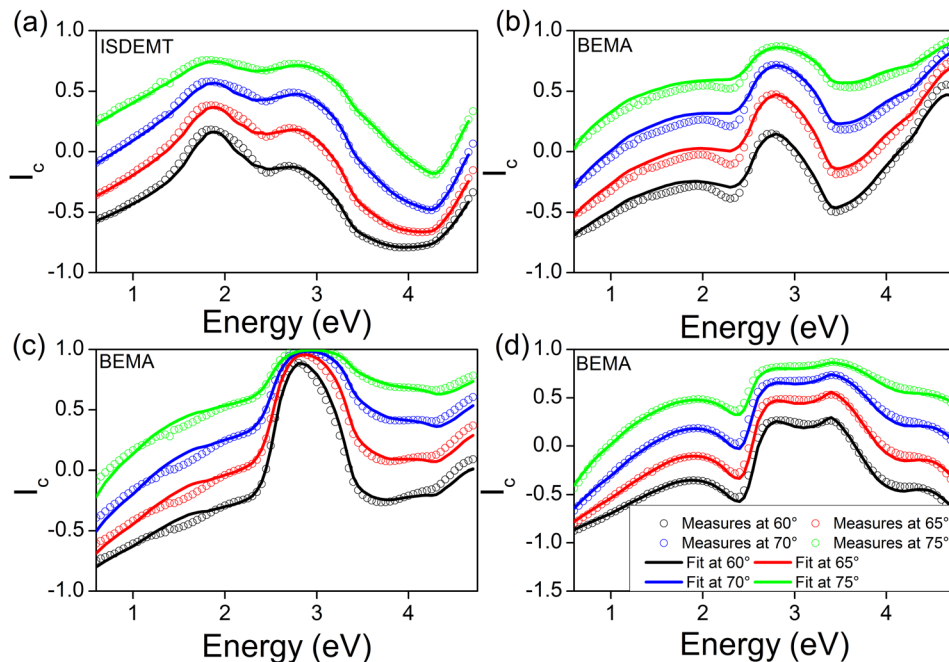


FIG. 4. Comparison between the measured (symbol) and calculated (solid lines) I_c ellipsometric parameters of (a) F1, (b) F2, (c) F3, and (d) F4. The measurements are performed at 4 angles of incidence: 60°, 65°, 70°, and 75°.

position, the orientation, and the size of Au nanoparticles, as well as the sublayer thicknesses are set to the values deduced from TEM images (Fig. 1). The thicknesses of L1, L2, and L3 sublayers of F1 are 56 nm, 12 nm, and 52 nm, respectively. Note that the NP size along the \mathbf{e}_3 axis is assimilated to the thickness of L2. The ellipsometric parameters, I_s and

I_c , are then calculated by using the Berreman transfer matrix formalism.³⁹

To find the best way to model ellipsometric spectra, the root mean square errors (rmse) between the measured and calculated ellipsometric spectra are reported in Fig. 5. The rmse is evaluated by using the following equation:

$$rmse = \sqrt{\frac{1}{8N} \sum_{i=1}^4 \sum_{j=1}^N (I_s(\lambda_j, \theta_i) - I_{s1}(\lambda_j, \theta_i))^2 + (I_c(\lambda_j, \theta_i) - I_{c1}(\lambda_j, \theta_i))^2}, \quad (18)$$

where λ_j are the wavelengths used for measurements. θ_i are the angles of incidence while (I_{s1}, I_{c1}) and (I_s, I_c) are the calculated and measured ellipsometric parameters, respectively. As shown in Fig. 5(a), the MG effective medium theory fails to describe the optical properties of F1, especially close to the plasmon band of NPs [Fig. 5(b)]. Indeed, this theory is not relevant for non-spherical NPs as those observed in TEM images. In addition, the MG theory is only valid for three-dimensional random or cubic organization of NPs. The best agreement between the F1 experimental and calculated spectra is found by using the ISDEMT theory suggesting that the optical properties of the medium composed of ellipsoidal NPs can be directly deduced from local TEM measurements by using the ISDEMT. This result highlights the importance of taking into account dipolar interactions, the shape distribution, and the orientation of NPs in the effective medium theory. Thus, the ISDEMT can be viewed as the relationship between the microscopic and the macroscopic properties of MIFs. For F2 and F3, the smallest rmse is obtained by using the BEMA theory [Figs. 5(a) and 5(c)]. Indeed, as revealed by TEM images (Fig. 1), F2 MIF consists of a percolated network of pseudodendritic nanostructures. Contrary to the ISDEMT, the geometry of the nanostructure is lost in the

BEMA theory. As expected by the BEMA theory, there is no longer distinction between the matrix and inclusion materials. On the other hand, the rmse calculated from the MG theory and the BEMA theory converges toward the same value for F4. For this sample, the Au volume fraction of L2 found by both models is 100% and the dielectric function of L2 is equal to the dielectric function of Au. Note that in our case, the NPs are embedded in a homogeneous medium. Several studies have investigated the optical properties of NPs supported on a substrate. Two approaches are used to model the optical properties of NPs supported on a surface: the Yamaguchi⁴⁰ model and the Bedeaux and Vlieger model.⁴¹ The first one is based on point dipole approximation. It takes into account the presence of the substrate interface by introducing some virtual dipole images. The NPs, in the Bedeaux and Vlieger model, are assimilated as an excess of surface susceptibility on the substrate. Thus, the presence of the substrate is a strong contribution to the plasmonic properties of NPs. Since the NPs considered in this paper are embedded in a homogeneous dielectric medium, no contribution from image dipoles has been taken into account in our calculations. In other words, the proposed models must be improved to introduce the substrate interface effects.

In the following, the F1 ellipsometric spectra is exploited with the ISDEMT model while the Bruggeman effective medium theory is used to analyze the F2, F3, and F4 spectra. As shown in Figs. 3 and 4, a good agreement is obtained between the experimental spectra and the calculated ones. Small deviations only observed on the F2 and F3 I_s spectra in the 0.6 eV–1.7 eV spectral range could be due to multipolar effects,⁴² which appear for a high volume fraction of the Au nanostructure.

The evolutions of the L2 film thickness and Au volume fraction with the nominal MIF thickness (h_0) are reported in Fig. 6. The L2 thickness of F2 determined from ellipsometry is close to the value deduced from TEM confirming that the BEMA is suitable for modeling the optical properties of the L2 layer of F2. As expected, the volume fraction increases monotonously with the deposition time until a dense Au film is formed. However, the variations of the L2 film thickness are more tedious and can be explained by a competition between the lateral and the vertical growth of gold nanostructures. Indeed, as pointed out previously,⁷ at the beginning of the deposition, Au adatoms migrate on the SiO_2 surface until

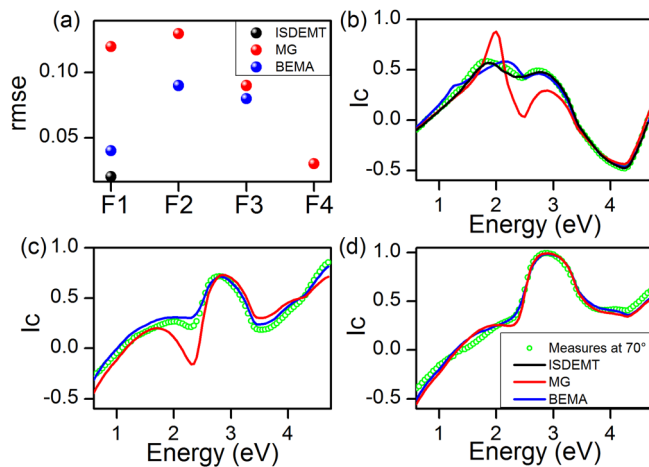


FIG. 5. (a) Comparison between the rmse obtained from the ISDEMT, BEMA, and MG models. (b)–(d) Comparison between the measured I_c parameter and the calculated ones from the ISDEMT, BEMA, and MG models for (b) F1, (c) F2, and (d) F3 films. The ISDEMT is only applied for the F1 film.

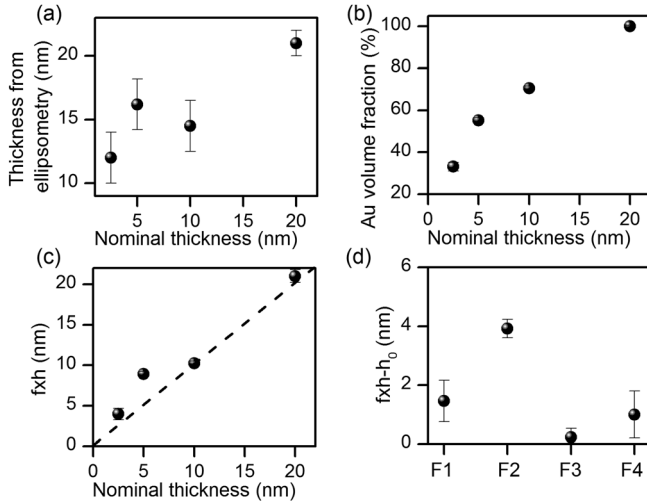


FIG. 6. Evolution of (a) the thickness estimated by ellipsometry, (b) the Au volume fraction, and (c) the product $f \times h$ with the nominal thickness h_0 of the L2 layer. The dashed line in (c) is only used as a guideline. (d) Deviation between the product $f \times h$ estimated from ellipsometry and the nominal thickness h_0 for F1, F2, F3, and F4 films.

they nucleate on other adatoms, resulting in the formation of Au NPs (Film F1) through a Volmer-Weber growth mode. This mode occurs when adatoms are more strongly bounded to each other than with the substrate. This leads to the formation of NPs instead of a uniform dense layer. Further deposition fills the empty space between NPs with few modifications of the film thickness until the NPs begin to agglomerate each

other to form a percolated network (film F2 and F3). As the F1, F2, and F3 films are composed of a mixture of Au and SiO_2 , their nominal thickness determined from gravimetric measurements is underestimated. Once the SiO_2 surface is completely covered, the film thickness takes the same value as the nominal one (film F4) and starts to increase linearly with the deposition time through a Frank-Van der Merwe growth mode.⁷ This growth mode occurs when adatoms are strongly bounded to the substrate. This is the case for long deposition time in which the thick gold film can be assimilated to the substrate. This leads to a layer-by-layer film growth.

In the framework of this growth mechanism, the nominal Au thickness h_0 is linked to the volume fraction f and the film thickness h is determined from ellipsometry by the following relationship:

$$h_0 = fh. \quad (19)$$

Figure 6(c) shows the product of the Au volume fraction and the L2 thickness determined by ellipsometry as a function of the nominal Au thickness. The deviation between the product fh and h_0 is also shown in Fig. 6(d) for all films. As expected by Eq. (19), a linear relationship with a slope close to 1 is observed between both quantities.

Ellipsometry enables the determination of the optical properties of the L2 layer. The effective dielectric tensor of the L2 sublayer of F1 is determined by combining the ISDEMT model and TEM. As shown in Fig. 7, it has the following symmetry:

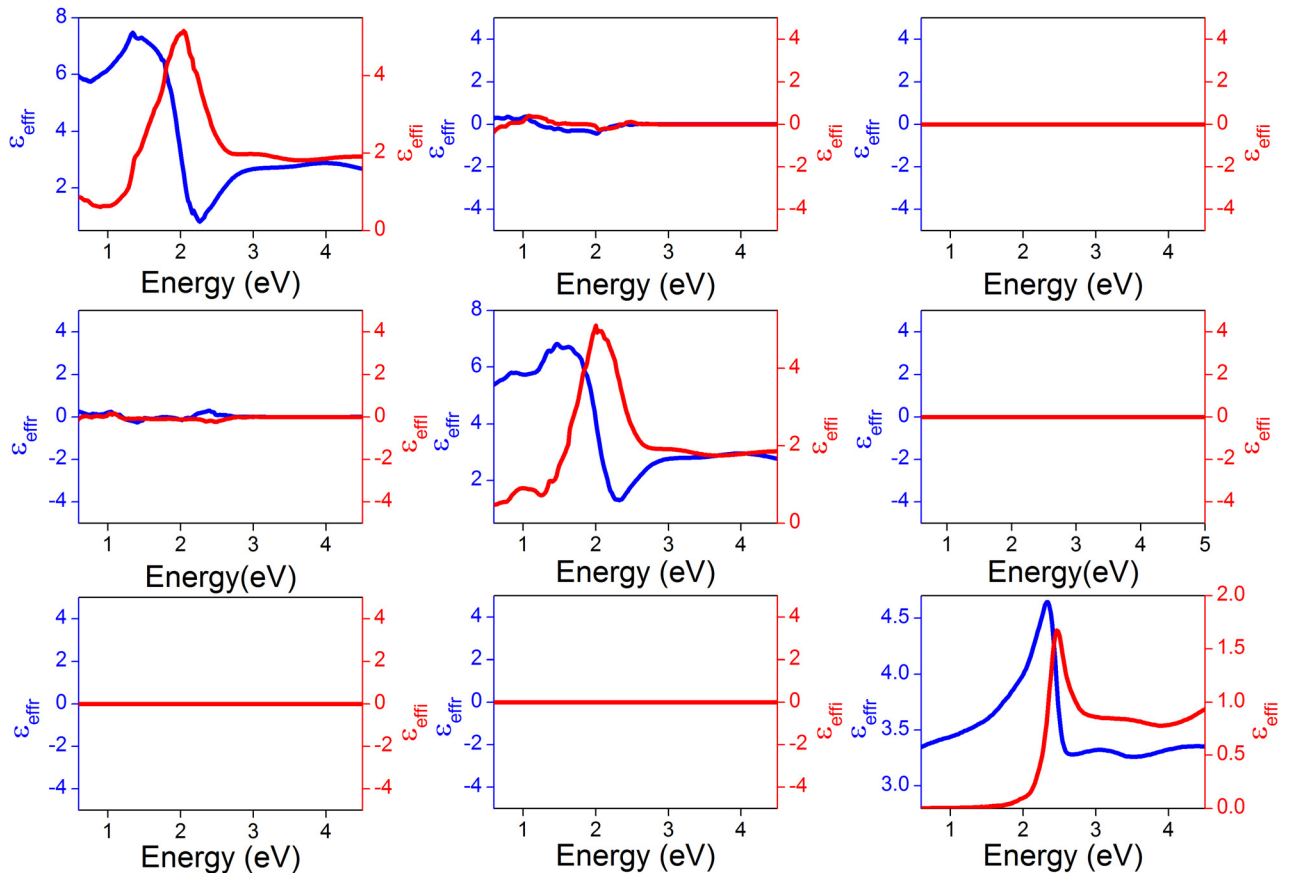


FIG. 7. Real (ϵ_{effr}) and imaginary (ϵ_{effi}) parts of the effective dielectric tensor of the L2 layer of F1.

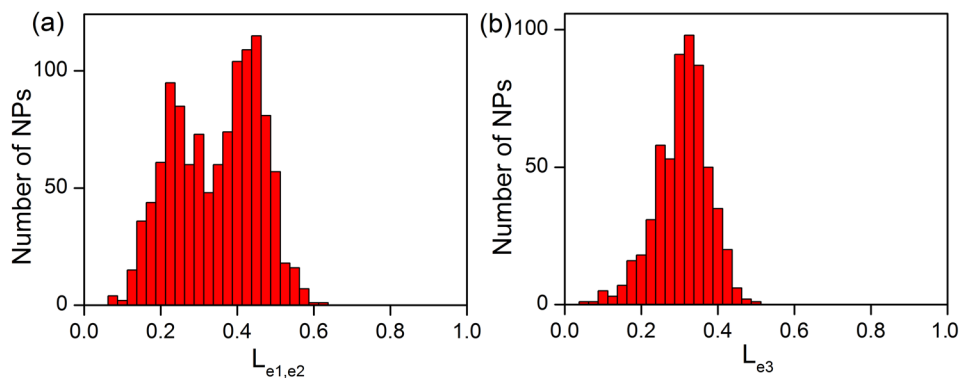


FIG. 8. Distribution of the depolarization parameters of F1 Au NPs (a) in the $(\mathbf{e}_1, \mathbf{e}_2)$ plane and (b) along the \mathbf{e}_3 axis.

$$[\epsilon_{eff}] = \begin{pmatrix} \epsilon_o & 0 & 0 \\ 0 & \epsilon_o & 0 \\ 0 & 0 & \epsilon_e \end{pmatrix}, \quad (20)$$

where ϵ_o and ϵ_e are the ordinary and extraordinary effective dielectric function, respectively. Thus, this film can be considered as a uniaxial medium with an optical axis oriented along the direction \mathbf{e}_3 , confirming that NPs have a random in-plane orientation [Fig. 2(c)]. The absence of an in-plane orientation of NPs is also confirmed by recording ellipsometric measurements at several azimuths of the plane of incidence (not shown).

The interband transition threshold, located at 2.5 eV, is clearly observed on the imaginary part of ϵ_o and ϵ_e . For energy higher than the interband transition threshold, the dielectric tensor is roughly dispersionless. In the visible spectral range, the imaginary parts of the ordinary and extraordinary effective dielectric functions of F1 are dominated by a strong plasmon band centered at 2.02 eV and 1.66 eV, respectively. This splitting is a consequence of the in-plane organization of gold NPs and the asymmetric interaction between them. Indeed, due to the small interparticle distance, the electric fields generated by a polarized NP interact strongly with the adjacent NPs. If the nanoparticles are excited by an incident field parallel to the $(\mathbf{e}_1, \mathbf{e}_2)$ plane, the electric field induced by the excited dipoles reduces the restoring force of electrons, resulting in a redshift of the plasmon resonance. On the contrary, if the incident electric field is parallel to the \mathbf{e}_3 axis, the field generated by the excited dipoles enhances the restoring force of electrons, resulting in a blueshift of the plasmon resonance.^{43–45} Moreover, the plasmon band of the ordinary effective dielectric function is broader than the plasmon band of the extraordinary effective dielectric function. The width of the plasmon band is mainly related to the inhomogeneous broadening induced by the shape distribution.³¹ To explain this broadening, the distribution of the depolarization parameter ($L_{e1,e2}$) in the $(\mathbf{e}_1, \mathbf{e}_2)$ plane, determined by combining TEM measurements (Fig. 1) and Eq. (10), is compared to the distribution of the depolarization parameter (L_{e3}) along the \mathbf{e}_3 direction (Fig. 8). $L_{e1,e2}$ follows a bimodal distribution, while a narrow distribution centered at 0.33 is obtained for L_{e3} . Indeed, NPs which are assimilated to ellipsoids, have two of their principal axes in the $(\mathbf{e}_1, \mathbf{e}_2)$ plane. Thus, the effect of the NP shape distribution is more pronounced for the ordinary effective dielectric function. In accordance with the Kramers-Kronig

relations, a large variation of the real parts of the ϵ_o and ϵ_e is expected close to the plasmon resonance. The effective birefringence Δn and optical dichroism Δk of the film, defined as the difference between the extraordinary and the ordinary effective refractive indexes and extinction coefficients, respectively, are reported in Fig. 9. The effective dichroism is negative in the whole spectral range. In addition, the effective dichroism is maximal while the effective birefringence changes sign at 2.1 eV i.e., close to the plasmon energy of Au inclusions. Indeed, a negative birefringence is observed for lower energy than 2.1 eV, while the effective birefringence becomes positive for higher energy. Thus, the asymmetric dipolar interactions between NPs, as well as their in-plane orientation, induce anisotropic plasmonic properties.

The comparison between the effective dielectric function of all films is shown in Fig. 10. A broad plasmon band centered at 1.55 eV is also observed on the imaginary part of the dielectric function of F2. The width and the position of this plasmon band can be explained by considering the fractal shape of the Au nanostructure. As each nanostructure has specific depolarization parameters, the shape distribution induces an inhomogeneous broadening. In addition, as reported by several authors,^{46,47} a complex spatial distribution of the electric field with the presence of several hot spots occurs in this percolated Au nanostructure. The real part of the effective dielectric function is negative for smaller energy than 2.4 eV, suggesting that the film takes metallic properties. Thus, this film is a hybrid between a purely

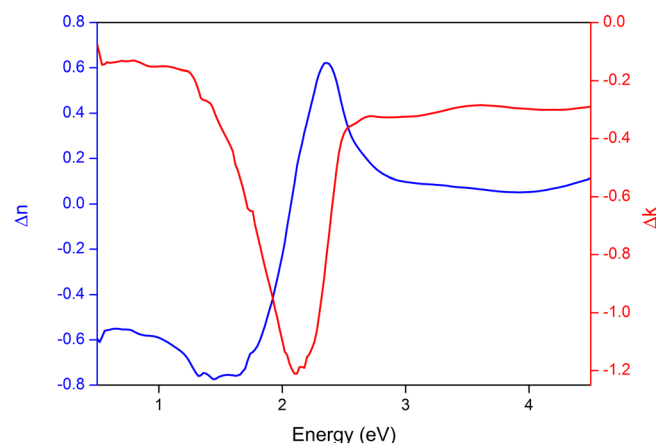


FIG. 9. Effective birefringence and dichroism of the L2 layer of F1.

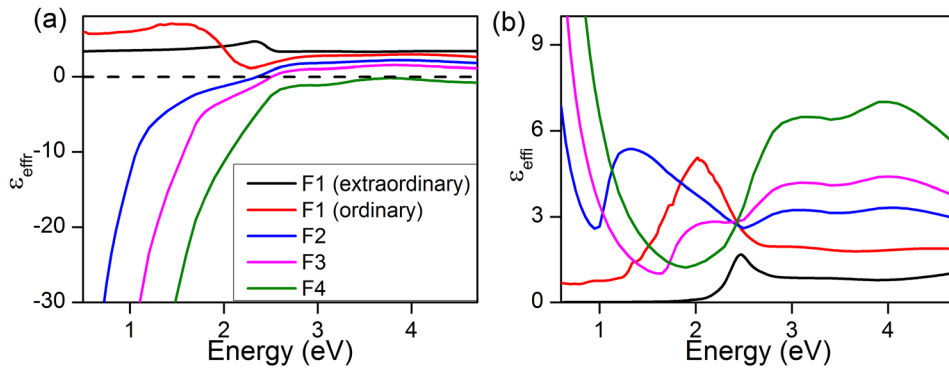


FIG. 10. (a) Real part and (b) imaginary part of the effective dielectric functions of F1, F2, F3, and F4.

metallic material and a plasmonic material. In accordance with TEM images, this result supports that this film is composed of a network of percolated gold nanostructure. Indeed, the volume fraction of Au in this film is higher than the percolation threshold estimated by ellipsometry at 36%. The real part of the effective dielectric functions of F3 and F4 is also negative. However, no plasmon band is observed in their effective dielectric function suggesting that no plasmon mode is coupled with the light. In other words, Au nanostructures disappear and the effective dielectric function of L2 tends toward the dielectric function of Au. This behavior is also confirmed by the blue shift of the plasma edge energy defined as the energy for which the real part of the effective dielectric function is equal to 0. Indeed, the plasma edge energy is sensitive to the average density of free electrons in the film.

To give more quantitative insights into the electronic properties of L2 films, we have evaluated their effective density of free electrons. By assuming that the effective dielectric function of L2 and the dielectric function of Au are both described by the Drude dispersion in the infrared spectral range, we can theoretically derive a linear relationship between the effective density of free electrons n in the L2 layer and the volume fraction f of Au above the percolation threshold⁴

$$\begin{cases} \frac{n - n_{Au}}{n_{Au}} = \frac{f - 1}{1 - f_s} & \text{if } f > f_s \\ n = 0 & \text{if } f \leq f_s, \end{cases} \quad (21)$$

where n_{Au} is the density of free electrons of Au. This value is estimated at $5.15 \times 10^{28} \text{ m}^{-3} \pm 1 \times 10^{26} \text{ m}^{-3}$ by fitting the tabulated dielectric function of Au by a Drude dispersion law.³⁸ The evolution of the density of electron with the volume fraction of gold is reported in Fig. 11. For an Au volume fraction smaller than the percolation threshold ($f < f_s$), the film, which is composed of isolated Au nanoparticles, can be considered as an insulator. Indeed, as reported by Hövel *et al.*,²⁵ the MIF, which can be modeled as metallic islands which interact capacitively, has a zero dc-conductivity. Therefore, the real part of the effective dielectric tensor is positive and the effective density of free electrons is equal to 0. At the percolation threshold of Au ($f = f_s$), an insulator-metal transition occurs. Above the percolation threshold ($f > f_s$), the effective density of free electrons increases with the Au volume fraction according to Eq. (21) until it reaches

the bulk value. In other words, the film becomes more and more conductive as the volume fraction increases. Therefore, the volume fraction of Au is a significant factor controlling the electronic properties of films. By considering the symmetry of the BEMA equation, the percolation threshold of SiO_2 is equal to $1 - f_s$, suggesting that for a higher volume fraction of Au, the film can be assimilated as isolated SiO_2 nanostructures in the Au matrix. This behavior is in agreement with the decrease of rmse calculated from the MG model for the F3 film. In other words, the F3 film, which has a Au volume fraction higher than $1 - f_s$, can be viewed as a 3-dimensional material with spherical SiO_2 inclusions embedded in a gold matrix.

V. CONCLUSIONS

In summary, we have investigated the growth mechanism of Au films sandwiched between two SiO_2 layers by combining TEM and spectroscopic ellipsometry. We demonstrate that the growth mechanism involves a Volmer-Weber growth mode. In addition, the optical properties of Au/ SiO_2 films are correlated to their nanostructures by analyzing the ellipsometric spectra with three effective medium theories. The choice of the effective medium theory depends on the morphology of Au nanostructures. For an Au volume fraction smaller than the percolation threshold, the film is composed of a two-dimensional array of ellipsoidal NPs and its optical properties can be modeled by the ISDEMT. This film

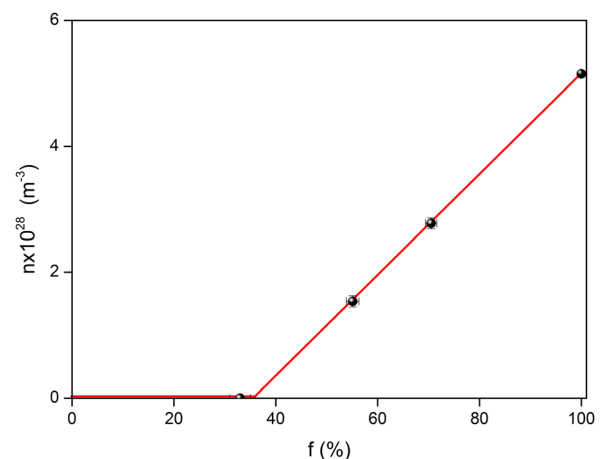


FIG. 11. Evolution of the effective density of free electrons in the L2 layer with the volume fraction of Au.

exhibits anisotropic plasmonic properties, which come from asymmetric dipolar interactions between NPs. Close to the percolation threshold, Au and SiO₂ share the same roles and the optical properties of the film can be described by the BEMA. The film simultaneously exhibits metallic and plasmonic properties. However, for a high Au volume fraction, the BEMA and MG converge toward the same results, suggesting that the film is composed of isolated SiO₂ inclusion embedded in a gold matrix. The strong dependence between the volume fraction and the morphology of Au MIFs offers the opportunities to tune both their optical and electronic properties.

- ¹S. Berthier, *Optique Des Milieu Composites* (Polytechnica, France, 1993).
- ²A. J. De Vries, E. S. Kooij, H. Wernmeester, A. A. Mewe, and B. Poelsema, *J. Appl. Phys.* **101**, 053703 (2007).
- ³V. Sabayev, N. Croitoru, A. Inberg, and Y. Shacham-Diamand, *Mater. Chem. Phys.* **127**, 214 (2011).
- ⁴S. Berthier, K. Driss-Khodja, and J. Lafait, *J. Phys.* **48**, 601 (1987).
- ⁵V. Švorcák, J. Siegel, P. Šutta, J. Mistrík, P. Janíček, P. Worsch, and Z. Kolská, *Appl. Phys. A* **102**, 605 (2011).
- ⁶R. W. Coehrn, G. D. Cody, M. D. Coutts, and B. Abeles, *Phys. Rev. B* **8**, 3689 (1973).
- ⁷J. Sukmanowski, Y. Battie, F. X. Royer, and A. En Naciri, *J. Appl. Phys.* **112**, 103536 (2012).
- ⁸S. Ducourtieux, V. A. Podolskiy, S. Grésillon, S. Buil, B. Berini, P. Gadenne, A. C. Boccara, J. C. Rivoal, W. D. Bragg, K. Banerjee, V. P. Safonov, V. P. Drachev, Z. C. Ying, A. K. Sarychev, and V. M. Shalaev, *Phys. Rev. B* **64**, 165403 (2001).
- ⁹H. Sun, M. Yu, G. Wang, X. Sun, and J. Lian, *J. Phys. Chem. C* **116**, 9000 (2012).
- ¹⁰E. Cottancin, J. Lermé, M. Gaudry, M. Pellarin, J.-L. Vialle, M. Broyer, B. Prével, M. Treilleux, and P. Mélinon, *Phys. Rev. B* **62**, 5179 (2000).
- ¹¹H. A. Chen, J. L. Long, Y. H. Lin, C. J. Weng, and H. N. Lin, *J. Appl. Phys.* **110**, 054302 (2011).
- ¹²P. Pavaskar, I. K. Hsu, J. Theiss, and W. H. Hung, *J. Appl. Phys.* **113**, 034302 (2013).
- ¹³S. Buil, J. Aubineau, J. Laverdant, and X. Quélin, *J. Appl. Phys.* **100**, 063530 (2006).
- ¹⁴M. Breit, V. A. Podolskiy, S. Grésillon, G. von Plessen, J. Feldmann, J. C. Rivoal, P. Gadenne, A. K. Sarychev, and V. M. Shalaev, *Phys. Rev. B* **64**, 125106 (2001).
- ¹⁵A. K. Sarychev, V. A. Shubin, and V. M. Shalaev, *Phys. Rev. B* **60**, 16389 (1999).
- ¹⁶J. Sancho-Parramon, V. Janicki, and H. Zorc, *Opt. Express* **18**, 26915 (2010).
- ¹⁷M. R. Gartia, A. Hsiao, A. Pokhriyal, S. Seo, G. Kulsharova, B. T. Cunningham, T. C. Bond, and G. L. Liu, *Adv. Opt. Mater.* **1**, 68 (2013).
- ¹⁸B. Abel, T. S. Kabir, B. Odukoya, M. Mohammed, and K. Aslan, *Anal. Methods* **7**, 1175 (2015).
- ¹⁹T. Karakouz, D. Holder, M. Goomanovsky, A. Vaskevich, and I. Rubinstein, *Chem. Mater.* **21**, 5875 (2009).
- ²⁰A. Monti, A. Toscano, and F. Bilotti, *J. Appl. Phys.* **121**, 243106 (2017).
- ²¹T. W. H. Oates and A. Mücklich, *Nanotechnology* **16**, 2606 (2005).
- ²²Y. Battie, A. En Naciri, W. Chamorro, and D. Horwat, *J. Phys. Chem. C* **118**, 4899 (2014).
- ²³Y. Battie, A. En Naciri, N. Chaoui, Y. Le Gall, D. Muller, M. Carrada, and D. Mathiot, *J. Appl. Phys.* **122**, 085308 (2017).
- ²⁴H. T. Beyene, J. W. Weber, M. A. Verheijen, M. C. M. Van De Sanden, and M. Creatore, *Nano Res.* **5**, 513 (2012).
- ²⁵M. Hövel, M. Alws, B. Gompf, and M. Dressel, *Phys. Rev. B* **81**, 035402 (2010).
- ²⁶M. Lončarić, J. Sancho-Parramon, and H. Zorc, *Thin Solid Films* **519**, 2946 (2011).
- ²⁷C. Pecharroman, E. Della Gaspera, A. Martucci, R. Escobar-Galindod, and P. Mulvaney, *J. Phys. Chem. C* **119**, 9450 (2015).
- ²⁸V. A. Markel, *J. Opt. Soc. Am. A* **33**, 1244 (2016).
- ²⁹Y. Battie, A. Resano-Garcia, N. Chaoui, Y. Zhang, and A. En Naciri, *J. Chem. Phys.* **140**, 044705 (2014).
- ³⁰Y. Battie, A. Resano-Garcia, A. En Naciri, S. Akil, and N. Chaoui, *Appl. Phys. Lett.* **107**, 143104 (2015).
- ³¹A. Resano-Garcia, Y. Battie, A. En Naciri, S. Akil, and N. Chaoui, *J. Chem. Phys.* **142**, 134108 (2015).
- ³²Y. Battie, I. Izquierdo-Lorenzo, A. Resano-Garcia, A. E. Naciri, S. Akil, P. M. Adam, and S. Jradi, *J. Nanopart. Res.* **18**, 217 (2016).
- ³³J. Toudert, L. Simonot, S. Camelio, and D. Babonneau, *Phys. Rev. B* **86**, 045415 (2012).
- ³⁴J. Toudert, D. Babonneau, L. Simonot, S. Camelio, and T. Girardeau, *Nanotechnology* **19**, 125709 (2008).
- ³⁵E. Detsi, M. Salverda, P. R. Onck, and J. T. M. De Hosson, *J. Appl. Phys.* **115**, 044308 (2014).
- ³⁶Y. Yagil, P. Gadenne, C. Julien, and G. Deutscher, *Phys. Rev. B* **46**, 2503 (1992).
- ³⁷R. Batabyal, J. C. Mahato, D. Das, A. Roy, and B. N. Dev, *J. Appl. Phys.* **114**, 064304 (2013).
- ³⁸E. D. Palik, *Handbook of Optical Constants of Solids* (Academic Press, Orlando, 1985).
- ³⁹M. Schubert, *Phys. Rev. B* **53**, 4265 (1996).
- ⁴⁰T. Yamaguchi, S. Yoshida, and A. Kinbara, *Thin Solid Films* **21**, 173 (1974).
- ⁴¹D. Bedeaux and J. Vlieger, *Optical Properties of Surfaces* (Imperial College Press, London, 2002).
- ⁴²I. Romero, J. Aizpurua, G. W. Bryant, and F. J. G. De Abajo, *Opt. Express* **14**, 9988 (2006).
- ⁴³T. W. H. Oates, H. Wormeester, and H. Arwin, *Prog. Surf. Sci.* **86**, 328 (2011).
- ⁴⁴W. Rechberger, A. Hohenau, A. Leitner, J. R. Krenn, B. Lamprecht, and F. Aussenegg, *Opt. Commun.* **220**, 137 (2003).
- ⁴⁵M. Arya, M. Ranjan, M. Bhatnagar, R. Nath, and A. Mitra, *Plasmonics* **1**, 1 (2017).
- ⁴⁶K. Seal, M. A. Nelson, Z. C. Ying, D. A. Genov, A. K. Sarychev, and V. M. Shalaev, *Phys. Rev. B* **67**, 035318 (2003).
- ⁴⁷S. Grésillon, L. Aigouy, A. C. Boccara, J. C. Rivoal, X. Quelin, C. Desmarest, P. Gadenne, V. A. Shubin, A. K. Sarychev, and V. M. Shalaev, *Phys. Rev. Lett.* **82**, 4520 (1999).